Journal of Materials Chemistry B

ROYAL SOCIETY OF CHEMISTRY

PAPER

View Article Online
View Journal | View Issue

Cite this: J. Mater. Chem. B, 2023, 11, 4318

Engineering ultrasound-activated piezoelectric hydrogels with antibacterial activity to promote wound healing†

Min Xu,[a] Shaozhen Wu,[e] Li Ding,[e] Caijiao Lu,[b] Huangjing Qian,[a] Jinmiao Qu *[c] and Yu Chen *[de]

Received 10th February 2023,
Accepted 22nd April 2023

DOI: 10.1039/d3tb00284e

rsc.li/materials-b

The development of nanocomposite hydrogel dressings with adhesion and superior mechanical and wound infection inhibition characteristics for wound repair and skin regeneration is urgently needed for clinical applications. In this study, the adhesive piezoelectric antibacterial hydrogels with high expansibility, degradability, and adjustable rheological properties were innovatively prepared by a simple assembly process with carboxymethyl chitosan (CMCS), tannic acid (TA), carbomer (CBM), and piezoelectric $FeWO_4$ nanorods. As an exogenous mechanical wave, ultrasound can trigger the piezoelectric effect of $FeWO_4$ and then effectively augment the generation of reactive oxygen species, exhibiting a superior antibacterial efficiency and preventing wound infection. *In vitro* and *in vivo* results have demonstrated that piezoelectric hydrogels can accelerate full-thickness skin wound healing in bacteria-infected mice by skin regeneration, inhibiting inflammatory response, increasing collagen deposition, and promoting angiogenesis. Such a discovery provides a representative paradigm for the rational design of piezoelectric hydrogel and effectively serves antibacterial and wound dressing fields.

1. Introduction

The skin is the first line of protection between the human body and the outside that can be easily damaged by the external environment.[1] The skin can effectively provide a barrier between the body and the outside environment to protect against infections and avoid infection, as well as maintain the stability of the internal environment.[2] Wound healing is a complicated process composed of the three stages of inflammation, proliferation, and remodeling phase.[3] The speed of wound healing is affected by the age-dependence,[4] nutritional status, and bacterial infections.[5] As a typical category, bacterial infection, especially wound infections caused by *S. aureus*, would lead to delayed healing, tissue damage, and even the involvement of organs or death.[6] Therefore, eliminating microorganisms is a crucial step in promoting wound healing. Clinically, antibiotics are mainly administered or injected for the treatment of wound infections, but such topical drug concentrations may not reach the effective range of antibacterial activity, and cause allergic reactions as well as possible development of bacterial resistance. Therefore, dressings that are safe to use and work directly on the wound are garnering more attention. Antibacterial dressings can effectively destroy bacteria without harming the surrounding tissues, preventing bacterial infections from spreading to open wounds and accelerating the healing process.[7] Furthermore, due to superior mechanical properties, the desirable carrier performance and excellent biocompatibility, the hydrogel is considered to be the ideal dressing material for wound healing and have received widespread attention.[8] By employing antibacterial, and anti-inflammatory properties and encouraging cell differentiation and proliferation through the mechanism of sustain-release biological activity substances in the wound, the hydrogel can aid in the healing of wounds.[9]

Chitosan is a natural polymer material obtained from the deacetylation of chitin. As a raw material of hydrogels, chitosan possesses excellent adhesion, biocompatibility, connecting regeneration, and antibacterial properties. In the process of wound healing, chitosan shows excellent hemostatic characteristics and promotes infiltration and migration of neutrophils and macrophages.[10] A variety of chitosan-based hydrogels that promote wound healing, such as lignin–chitosan–polyvinyl alcohol (PVA) composite hydrogels, have been developed.[11]

[a] Department of Operating Room, The First Affiliated Hospital of Wenzhou Medical University, Wenzhou, 325000, P. R. China
[b] Department of Wound Healing, The First Affiliated Hospital of Wenzhou Medical University, Wenzhou, 325000, P. R. China
[c] Department of Thyroid Cancer, The First Affiliated Hospital of Wenzhou Medical University, Wenzhou, 325000, P. R. China. E-mail: qujinmiao@126.com
[d] Materdicine Lab, School of Life Science, Shanghai University, Shanghai, 200444, P. R. China. E-mail: chenyuedu@shu.edu.cn
[e] Wenzhou Institute of Shanghai University, Wenzhou, 325000, P. R. China

† Electronic supplementary information (ESI) available. See DOI: https://doi.org/10.1039/d3tb00284e

However, the poor mechanical properties and acidic-activated antibacterial properties limited the application of chitosan. Carboxymethyl chitosan (CMCS) is a water-soluble chitosan derivative that retains the biological activity of chitosan while having good water absorption and retention capabilities. In addition, the carboxymethyl group is an active one that readily reacts with other molecules to provide the substance with new functionalities. As a high-quality drug carrier and hydrogel matrix, carbomer (CBM) is a synthetic polymer with the benefits of high viscosity, superior thermal stability, and outstanding histocompatibility.[12,13] A hydrogel based on the carbomer has been applied to save the zone of stasis in burn wounds[14] and to accelerate wound healing.[15,16] Tannic acid (TA), a polyhydroxy plant polyphenol with high antioxidant, antibacterial and anti-tumor properties, is made up of repeating units such as glucose and gallic acid.[17] It is known that phenolic hydroxyl groups allow TA to interact non-covalently with other polymers.[18] Besides, TA also has antibacterial and hemostatic properties.[19,20] The hemostatic and antibacterial capabilities of CMCS can be enhanced by the use of TA as a crosslinking agent. It can also stimulate angiogenesis and collagen precipitation.[21] Hydrogels formed by TA and CMCS are a potential option for the advancement of full-thickness wound healing.

Wound healing products that aim to treat bacterial wound infection are still missing, despite advancements in the creation of antibacterial materials with broad-spectrum antibacterial capabilities, such as nanofibers and nano-silver.[22] Numerous types of nanomaterials, including carbon-based nanomaterials such as carbon nanotubes and graphene oxide[23] and semiconductor nanoparticles, have been researched for their ability to fight against bacterial infection and speed up wound healing. The antibacterial activity of nanomaterials can be attributed to the inhibition of bacterial metabolism[24] or oxidative stress.[25] Piezoelectric material is a dielectric material with an asymmetric crystal structure. When subjected to external mechanical stress, piezoelectric material can form a dynamic internal electric field and surface potential, so that e^- and h^+ can be continuously separated and attracted to opposite surfaces for the redox reaction.[26] Piezoelectric catalysis can generate reactive oxygen species (ROS) by generating charge carriers that react with surrounding H_2O and O_2 molecules under the activation of ultrasound.[27] In this work, the distinct piezoelectric composite hydrogels with antibacterial function were innovatively prepared by cross-linking CMCS with carboxymethyl chitosan, TA, carbomer, and piezoelectric $FeWO_4$ antibacterial agent to accelerate wound healing. $FeWO_4$ nanorod with appropriate size has unique physicochemical properties, such as a high specific surface-to-volume ratio and suitable size, allowing for their greater mobility and passing through the cell biological membranes. Rheological and swelling properties, tissue adhesiveness, antibacterial behaviors, blood compatibility, and cytocompatibility were systematically studied. Additionally, collagen metabolism, histomorphological analysis, immunofluorescence staining, and wound closure were used to assess the stimulating effects of the hydrogel on a full-thickness wound repair model in mice.

2. Experimental

2.1 Synthesis of the CBM-CMCS-TA/FWO hydrogel

(a) Synthesis of $FeWO_4$ nanorods. The synthesis of $FeWO_4$ nanorods was based on a hydrothermal process. 3 mmol $(NH_4)_2Fe(SO_4)_2{\cdot}6H_2O$ (99.5%, MACKLIN) and 3 mmol $Na_2WO_4{\cdot}2H_2O$ (99.5%, MACKLIN) were dissolved in deionized water under magnetic stirring. Afterwards, $Na_2WO_4{\cdot}2H_2O$ solution was carefully added dropwise into the $(NH_4)_2Fe(SO_4)_2{\cdot}6H_2O$ solution under mild agitation, and the final volume of the mixture was 30 mL. The pH was then adjusted to 9.0 with 5 M NaOH. The final suspension was transferred into a 50 mL Teflon-lined stainless-steel autoclave and heat-treated at 160 °C for 24 h. After the system was cooled to room temperature naturally, collecting the products and washed with absolute ethanol and deionized water for several times, and then dried at 60 °C for 4 h in an oven (Fig. S1, ESI†).

(b) Synthesis of the CBM-CMCS-TA/FWO hydrogel. Briefly, carbomer 940 (Meilun Bio), carboxymethyl chitosan (MACKLIN), tannic acid (MACKLIN), and $FeWO_4$ nanorods were mixed under magnetic stirring at 50 °C, and then adjusted the pH to 7 with triethanolamine (MACKLIN) to give a 1% carbomer gel containing 0.1% (w/v) CMCS, 0.1% (w/v) TA and $FeWO_4$ nanorods. The final hydrogel was stored at 4 °C.

2.2 Characterization

Transmission electron microscopic (TEM) photographs were recorded on a Talos F200x G2 (FEI Company, USA) electron microscope (200 kV). Scanning electron microscopy (SEM) photographs were recorded on a field-emission SU8010 microscope (Hitachi, Japan). X-Ray photoelectron spectroscopy (XPS) spectra were collected on a K-Alpha Nexsa (Thermal Scientific, USA). The X-ray diffraction (XRD) patterns were determined on a D8 ADVANCE X-ray powder diffraction (Bruker, Germany) instrument using Cu Kα radiation (λ = 1.5406 Å) at 40 kV and 40 mA. Piezoresponse force microscopy (PFM) measurements were performed on an atomic force microscope (AFM) (Bruker Dimension Icon, Germany). The ESR characterization was performed on an electron paramagnetic resonance spectrometer (Bruker EMXplus-6/1, Bruker, Germany). The rheological properties of the hydrogel at variable frequencies and times were explored using a rheometer system (HAAKE MARS 40, Thermal Scientific, USA). The evolution of the storage and loss moduli was determined at a constant strain of 1% and a constant angular frequency of 1 rad s^{-1}. Thermogravimetric analysis (TGA) was performed on a TGA2 thermogravimetric analyzer (METTLER TOLEDO, USA) in a nitrogen atmosphere (nitrogen flow rate of 50 mL min^{-1}) with a heating rate of 10 °C min^{-1}. The scan range was between 30 and 700 °C.

2.3 Effect of $FeWO_4$ on the degradation of methylene blue (MB)

10 mg of $FeWO_4$ nanorods were dispersed in 50 mL methylene blue (MB, 10 mg mL^{-1}) aqueous solutions. Before the application of ultrasonic vibration, the aqueous dispersion was stirred for 30 min to establish adsorption–desorption equilibrium

between the $FeWO_4$ nanorods and MB molecules. The whole experiment was carried out in the dark to eliminate the influence of photocatalysis. The aqueous dispersion (5 mL) was collected at intervals and centrifuged to obtain a clear supernatant after US irradiation (1.0 MHz, 1 W cm^{-1}, 50% duty cycle). The clear supernatant was analyzed by UV-VIS-NIR spectroscopy (UV-3600 i Plus, Shimadzu, Japan).

2.4 Adhesive strength of the hydrogels

The adhesive ability of the hydrogels to the host tissue was studied using fresh porcine skin. The fresh porcine skin tissue was cut into 10 mm × 10 mm rectangles and immersed into phosphate buffer saline (PBS) before use. 100 μL of hydrogel was applied on the surface of the skin tissue and another skin tissue was put onto the hydrogel. The adhesion properties were tested using the lap-shear test on a dynamic and static testing machine (ETM 5001, GUOLIANG, China) equipped with a 50 N load cell at a rate of 2 mm min^{-1}.

2.5 *In vitro* antibacterial activity test

In this experiment, 100 μL of bacterial suspension (10^8 CFU mL^{-1}) was inoculated on 6 well cell culture plates. The samples were treated with the untreated control, US irradiation (1.0 MHz, 50% duty cycle, 5 min), CBM-CMCS-TA/FWO2 hydrogel, and CBM-CMCS-TA/FWO2 hydrogel + US irradiation (1.0 MHz, 50% duty cycle, 5 min), respectively. Then, the samples were exposed to a solid medium and the total number of colonies was calculated to evaluate the bacteriostatic effect after the bacteria continued to grow for 0.5 h and 4 h, respectively.

A live/dead bacteria staining kit was used to carry out the live/dead staining assay. Two fluorescent dyes were included in the kit. Only intact bacteria were detected by the green dye, while only bacteria with a compromised cell membrane or wall were detected by the red dye. In a nutshell, 1 mL of 0.85% NaCl was added to 2 mL of *S. aureus* strain after it had been cultivated to the post-log phase. Then, the samples were treated with the untreated control, US irradiation (1.0 MHz, 50% duty cycle, 5 min), CBM-CMCS-TA/FWO2 hydrogel, and CBM-CMCS-TA/FWO2 hydrogel + US irradiation (1.0 MHz, 50% duty cycle, 5 min), respectively. The mixture was, accordingly, suspended in 0.85% NaCl and centrifuged at 5000*g* for 5 min after 4 h of culture. The suspensions were then concurrently dyed for 15 minutes in the dark with a live/dead dye solution. Following two rounds of 0.85% NaCl washing, the stained bacteria were examined under a fluorescence microscope.

The combination of CBM-CMCS-TA/FWO2 hydrogel and US-induced bacterial membrane damage against *S. aureus* was determined by scanning electron microscopy (SEM) analysis. The samples were treated with the untreated control, US irradiation (1.0 MHz, 50% duty cycle, 5 min), CBM-CMCS-TA/FWO2 hydrogel, and CBM-CMCS-TA/FWO2 hydrogel + US irradiation (1.0 MHz, 50% duty cycle, 5 min), respectively. Once the absorbance at 600 nm reached 0.3, *S. aureus* was statically grown in polylysine-coated slides in 24-well plates at 37 °C. The slides were given a gentle PBS wash before being exposed to 2.5% glutaraldehyde at 4 °C for 12 hours. Each sample was dehydrated in ethanol after being postfixed with 1% osmium tetroxide. The samples were coated with gold after vacuum freeze-drying and examined under a scanning electron microscope (SEM).

2.6 Swelling test

The hydrogel and 20 mL PBS (pH = 7.2) were added to sealed vials at 37 °C. After a certain period, the hydrogel was taken out of the solution for weighing. Then, the weight was compared with the initial weight to calculate the swelling rate.

2.7 Cell culture and *in vivo* cytotoxicity assay

The direct contact test of the hydrogel and L929 cells was used to determine the cytotoxicity of the hydrogel. L929 cells, purchased from SUNNCELL Biotechnology (Wuhan, China), were cultured in Dulbecco's modified Eagle's medium (DMEM, Gibco) containing 10% fetal bovine serum (FBS, Gibco) and 1% penicillin–streptomycin (Gibco) at 37 °C in a CO_2 incubator. The disinfected hydrogel was co-incubated with L929 cells preseeded in 96-well plates for 24 h. After 24 h, the medium was replaced with a new 100 μL DMEM medium, and then 10 μL Cell Counting Kit-8 (CCK-8) (Beyotime, China) was added to each hole and continued to incubate for 1 h at 37 °C in a CO_2 incubator. Afterwards, the microplate reader (Infinite E Plex, Tecan, Switzerland) was used to determine the absorbance of the solution at 450 nm. Similarly, the Calcein-AM/PI kit (Beyotime, China) was used in the 6-well plates to stain L929 cells, and then the inverted fluorescent microscope (TS2R-FL, Nikon, Japan) was used to take a photograph.

2.8 Hemolytic activity test of the hydrogels

Erythrocytes were diluted by PBS to a final concentration of 5% (v/v). 500 μL hydrogel and 500 μL erythrocytes were added to the 1.5 mL centrifugal tube, and it was then incubated in an incubator for 1 h at 37 °C with a shaking speed of 100 rpm. PBS buffer was used as a negative control, and 0.1% Triton X-100 was used as a positive control. The absorbance of the solution was read by a microplate reader (Infinite E Plex, Tecan, Switzerland) at 540 nm. The hemolysis percentage was calculated from the relation: Hemolysis (%) = $[(A_e - A_b)/(A_p - A_b)] \times 100\%$, where A_e was the absorbance value for the experiment group. A_p was the absorbance value for the Triton X-100 positive control and A_b was the absorbance value for the PBS-negative control.

2.9 *In vivo* wound-healing assay

Male Kunming mice, obtained from China, weighing 22–25 g and 5–6 week age were used for studies. The animal experiments were conducted with the approval of ethics by the Ethics Committee of Shanghai University. All mice were anesthetized with isoflurane and full-skin round wounds (diameter of 8 mm) were created on the backbones of the mice with an 8 mm punch. 50 μL of *S. aureus* (1×10^8 CFU mL^{-1}) was smeared on the surface of the wounds to establish the bacteria-infected mouse model. All mice were randomly divided into 5 groups, including Tegaderm™ film (Control), US, CBM-CMCS-TA,

CBM-CMCS-TA/FWO, and CBM-CMCS-TA/FWO + US. Each group contained five mice. A control and US group were added with 50 μL of PBS, then dressed with Tegaderm™ film (3M Health Care, USA), and another group was added with 50 μL of the hydrogel. The mice in these different groups were photographed to evaluate their healing efficacy. After treatment for 14 days, the tissues of the infected wound areas (diameter of 10 mm) were harvested for pathological histology analysis.

2.10 Histology and immunohistochemistry

To assess epidermal regeneration and inflammation in the wound area, skin samples were fixed in 4% paraformaldehyde for 1 hour, embedded in paraffin, and cross-sectioned into 4 μm thickness slices. After the slices had been obtained, they were stained with Haematoxylin-Eosin and Masson trichrome dye. Every slice was examined and captured on a camera under a microscope (IX53, Olympus, Japan).

The tissue sections were initially fixed and washed. Following rinsing, they were permeabilized for 10 minutes at room temperature with 0.03% Triton-X100 and then blocked for 30 minutes at 37 °C with 3% bovine serum albumin (BSA). The primary antibodies for TNF-α and CD31 (1 : 200, Abcam, USA) were each incubated on the sections overnight (at least 8 hours) at 4 °C. The fluorescent secondary antibody (Abcam, USA) was applied to the sections after rinsing, and they were then allowed to sit at room temperature for 1 hour. Hoechst 33342 (Sigma-Aldrich, USA) was used as a counterstain on the nuclei for 10 minutes at room temperature. The outcomes were looked at using a confocal microscope (Olympus, Japan). Three randomly chosen views of each specimen were used to evaluate the photos using Image-Pro Plus 6.0 (Media Cybernetics, USA) for microvessel density.

2.11 Statistical analysis

All the data in this study were statistically analyzed by Student's *t*-test (unpaired, two-tailed). The values were expressed as mean ± standard mean error (SEM), and $P < 0.05$ was considered statistically significant ($^{*}P < 0.05$, $^{**}P < 0.01$, $^{***}P < 0.001$).

3. Results and discussion

3.1 Synthesis and characterization of $FeWO_4$ nanorods

The transmission electron microscopy (TEM) image exhibits the rod morphology of $FeWO_4$ nanocrystals with a length of hundreds of nanometers (Fig. 1a). The lattice fringe of 0.238 nm in the high-resolution TEM (HRTEM) image was

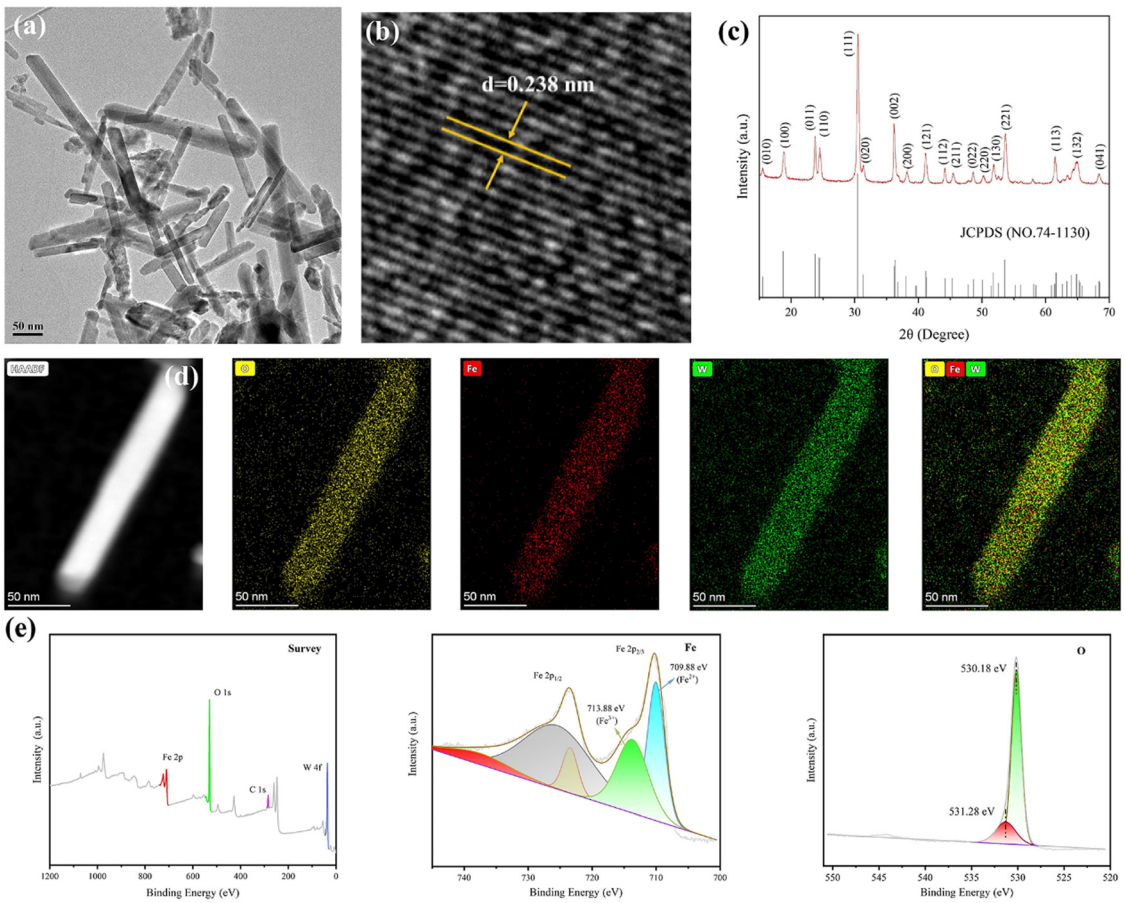

Fig. 1 Characterization of $FeWO_4$ nanorods. (a) TEM image, (b) HRTEM image, and (c) XRD pattern of $FeWO_4$. (d) Scanning transmission electron microscopy (STEM) images and the corresponding elemental mapping images. (e) Survey XPS spectrum and high-resolution Fe 2p and O 1s spectra of $FeWO_4$.

assigned to the (020) diffraction plane of $FeWO_4$ nanorods (Fig. 1b). The corresponding crystal structure was confirmed by X-ray diffraction analysis. The characteristic diffraction peaks can be indexed to monoclinic $FeWO_4$ (JCPDS no. 74-1130), with lattice parameters of a = 4.73 Å, b = 5.703 Å, and c = 4.952 Å (Fig. 1c). The homogeneous distributions of O, Fe, and W were detected in the elemental mapping, confirming the successful synthesis of the products (Fig. 1d). The chemical composition and surface chemical state of the $FeWO_4$ nanorods were determined by X-ray photoelectron spectroscopy (XPS) (Fig. 1e). The survey spectrum revealed the presence of O, Fe, and W. In the high-resolution spectrum of Fe 2p, two sub-peaks at 713.88 and 709.88 eV are assigned to Fe^{3+} and Fe^{2+}, respectively. O 1s spectrum with the asymmetric feature can be divided into two peaks (530.18 eV and 531.28 eV), which are attributed to lattice oxygen and surface-adsorbed oxygen, respectively.

The piezoelectric properties of the $FeWO_4$ nanorods were confirmed by piezo-response force microscopy. The phase and amplitude curves are shown in Fig. 2a. A hysteretic amplitude-voltage curve with a butterfly loop shape was captured, which is a property of ferroelectric materials. Furthermore, the average phase contrast ($\approx 180^\circ$) confirmed the piezoelectricity of $FeWO_4$ nanorods. The absorbance intensities of methylene blue (MB) treated with the $FeWO_4$ + US group showed a significant decrease, demonstrating the generation of ROS (Fig. 2b). The ROS species produced by $FeWO_4$ nanorods with US irradiation were quantitatively verified using typical electron spin resonance (ESR) technique (Fig. 2c and d). Typically, $^{\bullet}OH$ and $^{\bullet}O_2^-$ were detected using 5,5-dimethyl-1-pyrroline-*N*-oxide (DMPO) as the capture agent. Compared with the US alone group, the intense peak intensities of $^{\bullet}OH$ and $^{\bullet}O_2^-$ are directly reflected in the $FeWO_4$ + US group, demonstrating the piezoelectric effect of $FeWO_4$ nanorods.

3.2 Characterization of CBM-CMCS-TA/FWO hydrogels

Considering the outstanding stability, excellent bio-adhesion, and high patient acceptance characteristics, CBM was chosen as the excipient of the hydrogel.[28] Moreover, due to the limited hemostatic and antibacterial properties of CMCS, TA was introduced to cross-link with CMCS by hydrogen bond.[21] At the same time, CBM molecules can not only form hydrogen bonds with hydroxyl groups as carboxyl donors but also link with CMCS in the form of hydrogen bonds.[16] To form the hydrogel with a three-dimensional network structure (Fig. S3, ESI†), CBM, CMCS, and TA should be first mixed uniformly, and then the coiled molecules are expanded by the addition of triethanolamine due to the mutual repulsive force of negative charges. Based on changing the amount of CMCS, a series of CBM-CMCS-TA/FWO hydrogels with excellent mechanical properties, biocompatibility, and antibacterial properties were prepared by introducing $FeWO_4$ nanorods as antibacterial agents. The surface of the hydrogels at the microscale was characterized by scanning electron microscopy (Fig. 3a), which demonstrated that CBM-CMCS-TA/FWO hydrogels have obvious macropores and three-dimensional interconnected network structure, indicating the exceptional structural stability. This structure can promote the flow of oxygen and nutrients.[29]

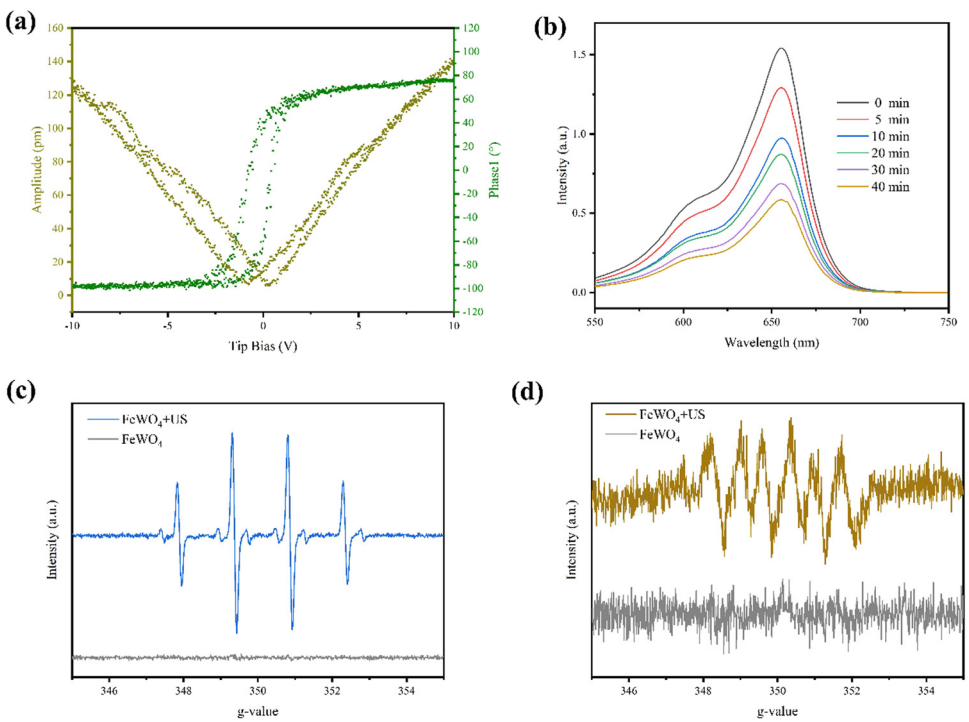

Fig. 2 Piezocatalytic performance under US irradiation. (a) Piezo-response of phase curve and amplitude curve of $FeWO_4$ nanorods. (b) Degradation of MB with different US irradiation time in the presence of $FeWO_4$. ESR spectra of $^{\bullet}OH$ (c) and $^{\bullet}O_2^-$ (d) under US irradiation.

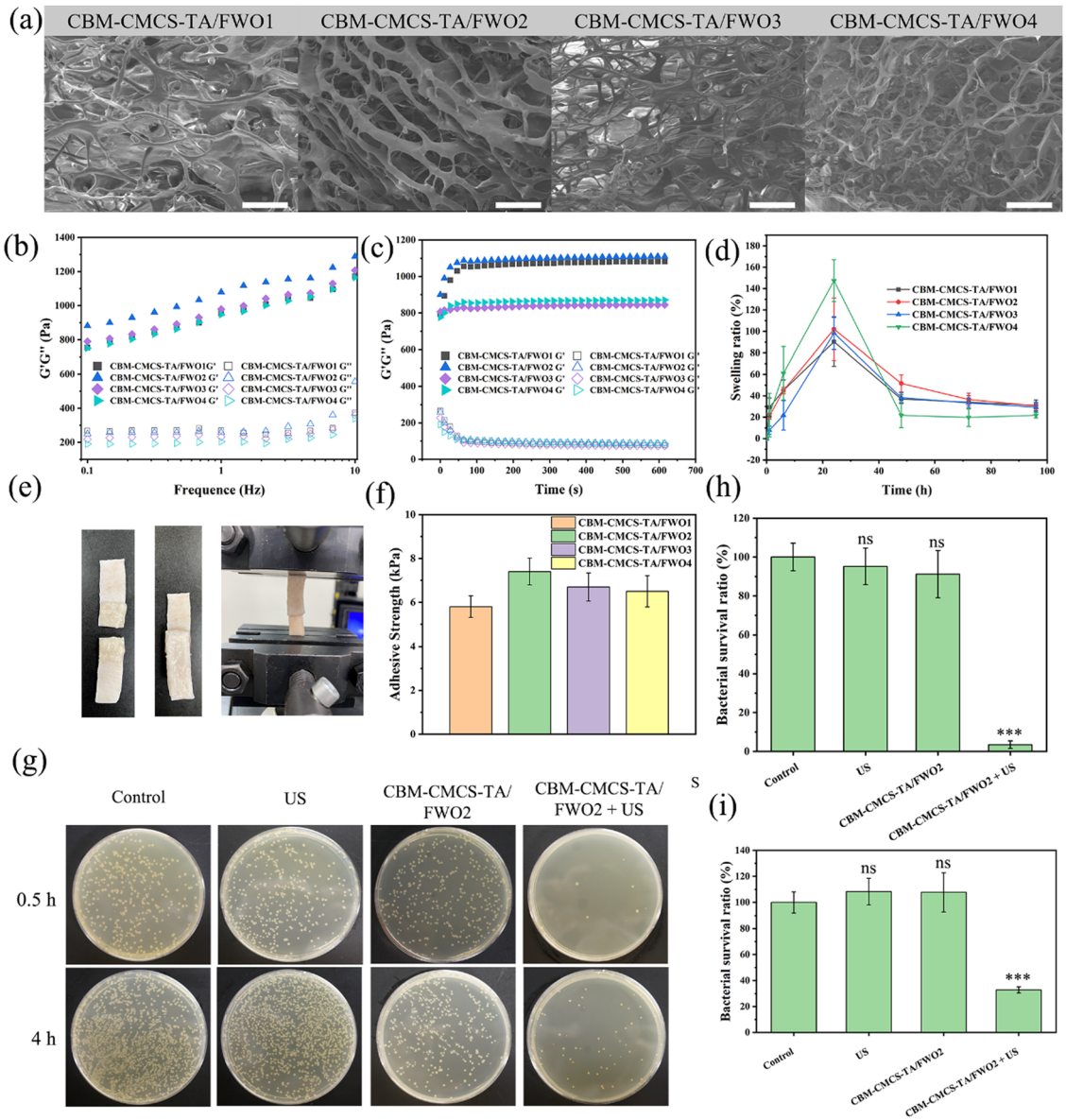

Fig. 3 Characterization and antibacterial performance of piezoelectric hydrogels. (a) SEM image of hydrogels with various CMCS ratios. The amounts of CMCS of CBM-CMCS-TA/FWO1, CBM-CMCS-TA/FWO2, CBM-CMCS-TA/FWO3, CBM-CMCS-TA/FWO4 are 0.05% (w/v), 0.1% (w/v), 0.2% (w/v) and 0.3% (w/v), respectively. Scale bar: 50 μm. Rheological of hydrogels with different frequencies (b) and time (c). (d) Swelling ratio of hydrogels in PBS (pH 7.4) at 37 °C. (e) Photographs of adhesive strength test. (f) Adhesive strength of hydrogels. (g) Photographs of *in vitro* antibacterial performance of hydrogels on LB agar plates after the bacteria continued to grow for 0.5 h and 4 h after various treatments, respectively. (h) Antibacterial properties of hydrogels of *in vitro* at 0.5 h. (i) Antibacterial properties of hydrogels of the live bacteria *in vitro* at 4 h. Data were expressed as mean ± S.E.M. ns indicates no significant difference. A significant difference at $^{*}P < 0.05$, $^{**}P < 0.01$, $^{***}P < 0.001$ level was compared with the control group.

The thermogravimetric analysis result in Fig. S2 (ESI†) also revealed the prominent thermal stability of the hydrogel.

The water uptake of the hydrogel accelerates the wound-healing process by absorbing wound effluence. The swelling performance of the hydrogel indicates that all the hydrogels reached the absorption maximum after 24 h (Fig. 3d). Meanwhile, the water absorption rate increased with the increase in the addition of CMCS. The curves of storage modulus (G') and loss modulus (G'') were recorded to analyze the effect of CMCS addition on the rheological properties of the hydrogels (Fig. 3b and c). In the time sweep test, the G' of hydrogels were all higher than G'', indicating the formation of a relatively stable hydrogel. At the same time, G' showed a trend of first increasing and then decreasing with the increase in the amount of CMCS, indicating that increasing a certain amount of CMCS can improve the crosslink density of hydrogels, but excessive CMCS will lead to the entanglement of uncrosslinked CMCS molecules and reduce the hydrogel stability. Similarly, in the frequency sweep test, the value of G' was greater than its corresponding value of G'' at frequencies between 0.1 and 10 Hz. Moreover, the addition of a certain amount of CMCS leads to a strong interaction between polymers and the increased cross-linking density of hydrogels.[30]

Aside from the components' positive effects on the wound-healing process, adhesion performance was also crucial.[31] The lap-shear test was used to evaluate the adhesion of hydrogels to skin the tissue (Fig. 3e). The adhesive strength of the prepared hydrogel was between 5.8 ± 0.49 and 7.4 ± 0.61 kPa, indicating that CBM-CMCS-TA/FWO hydrogel has superior adhesion performance (Fig. 3f), which can be attributed to the high viscosity of the polymers caused by the ionization of the carboxyl group of CBM.

3.3 Antibacterial activity

Due to the excellent ROS generation ability of $FeWO_4$ piezoelectric nanorods under US exposure, the antibacterial properties of the combination of hydrogels and antibacterial agent $FeWO_4$ were further studied. In this study, *in vitro* and *in vivo* antibacterial activity tests were used to evaluate its antibacterial properties. Counting of colony-forming units (CFU) was used to determine the bacterial survival rate of the killing effect of the hydrogel under US irradiation. After 5 min of US irradiation, the total number of *S. aureus* colonies in each hydrogel + $FeWO_4$ group was significantly reduced. Compared with the control group, the bacterial survival rate in the CBM-CMCS-TA/FWO2 hydrogel + US group was reduced to $32.77 \pm 2.39\%$ (Fig. 3g). In addition, there was no significant difference in bacterial survival between the US, CBM-CMCS-TA/FWO2 hydrogel and control groups ($P > 0.05$), suggesting that the bacterial lethality of hydrogels was due to the piezoelectric effect of $FeWO_4$. ROS generated by the piezoelectric effect can break through the threshold of cell survival and induce destructive cell damage, including loss of cell membrane integrity and intracellular protein leakage, and finally inducing irreversibly damage to bacteria.[32] Furthermore, the antibacterial activity of hydrogels against *S. aureus* was also tested at 4 h. As shown in Fig. 3h and i, the bacterial survival rate of the control group, US group, and CBM-CMCS-TA/FWO2 group was higher than the CBM-CMCS-TA/FWO2 + US group. These results confirmed that piezoelectric hydrogels with US have excellent antibacterial activity *in vitro*. In order to investigate the damage inflicted by the combination of CMCS-TA/FWO2 gel and US against *S. aureus*, live/dead staining assays were performed. In theory, living cells with intact cell membranes fluoresce bright green, while damaged cell membranes in dead cells fluoresce red. *S. aureus* treated with US were dyed green (live), which was comparable to the sample without any treatment and was consistent with the antibacterial activity analysis (Fig. S4, ESI†). As anticipated, there were significantly more bacteria dyed red (dead) in the samples treated with the CMCS-TA/FWO2 gel combined with US than in samples treated with other treatments, indicating that the CMCS-TA/FWO2 gel combined with US caused *S. aureus* cell wall injury and had a significant bactericidal effect on *S. aureus*.

SEM was used to further examine *S. aureus*' morphology and determine whether the CMCS-TA/FWO2 gel in conjunction with the US might have bactericidal activity. The untreated *S. aureus* was well-circumscribed with flat membrane surfaces that did not swell, as demonstrated in Fig. S5 (ESI†). The morphology of *S. aureus* in samples treated with US or the CMCS-TA/FWO2 gel was comparable to that of untreated bacteria. Furthermore, a damaged membrane with a deformed morphology appeared in *S. aureus* treated with the CMCS-TA/FWO2 gel in conjunction with US, which are signs of bacterial death. In contrast to bacteria treated with US or the CMCS-TA/FWO2 gel alone, as shown in Fig. S5 (ESI†), bacteria treated with the CMCS-TA/FWO2 gel and US together resulted in considerable bacteria death without maintaining the bacterial morphology. Our findings indicate that the use of the CMCS-TA/FWO2 gel in combination with US produced antibacterial properties that damaged bacterial membranes and caused bacterial death.

3.4 Biocompatibility evaluation of piezoelectric hydrogels

Excellent biocompatibility is an essential factor for the application of biomaterials. *In vitro* hemolysis test was performed to estimate the hemocompatibility of CBM-CMCS-TA/FWO hydrogel. Different from the positive control group with a bright red feature, the colors of the four hydrogel groups were similar to the PBS group, indicating no obvious hemolysis (Fig. 4b and Fig. S6, ESI†). The quantitative data are presented in Fig. 4a. All the hydrogel groups exhibited a very low hemolysis ratio ($<5\%$), indicating good hemocompatibility.[33] In order to evaluate the cytocompatibility of these hydrogels, a direct contact test between the L929 cells and hydrogels was carried out. There was no significant difference in cell viability between the hydrogel groups and the control group (Fig. 4c). Meanwhile, the live/dead cell staining assay also showed that no obvious dead cells were found in the four hydrogel groups (Fig. 4d). According to the results of Fig. 4c and d, the number of dead cells in the CBM-CMCS-TA/FWO3 group was higher than the other three groups. The above tests proved that these hydrogels have good biocompatibility. Ultimately, CBM-CMCS-TA/FWO2 with outstanding mechanical properties, rheological properties, and biocompatibility were selected for wound healing ability assessment.

3.5 *In vivo* wound healing in a full-thickness skin defect model and antibacterial effects

Motivated by the positive *in vitro* results, we looked more closely at the *in vivo* effects of CBM-CMCS-TA/FWO2 gel-mediated synergistic therapy on wound healing. To assess the effectiveness *in vivo*, a mouse full-thickness skin defect was performed (Fig. S7, ESI†). Fig. 5a–c illustrates that the wound areas became smaller in all four groups as postoperative time increased. As shown in Fig. 5a, mice in the CBM-CMCS-TA/FWO2 gel + US group had their wounds healed with the development of hair on the back after three sessions of the topical treatment. The wound closure rate was significantly improved with the CBM-CMCS-TA/FWO2 gel + US treatment, reaching 92.8% on day 14, compared to just 76.9% in the control group (Fig. 5a–c), demonstrating the superior ability of the CBM-CMCS-TA/FWO2 gel + US group to speed up the healing of wounds. The wound areas treated with CBM-CMCS-TA gel, CBM-CMCS-TA/FWO2 gel, and CBM-CMCS-TA/FWO2 gel + US were smaller than the Control and US groups after

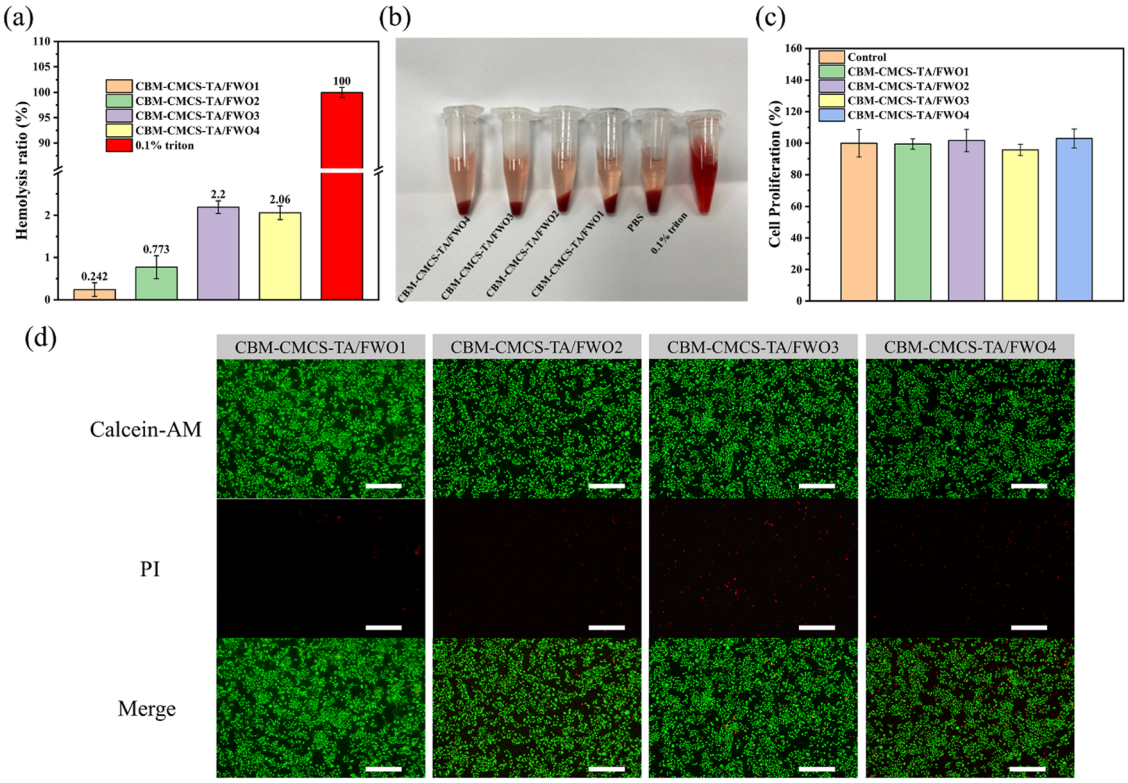

Fig. 4 Biological behavior assay of piezoelectric hydrogels. (a) Hemolytic percentage of the hydrogels. (b) Photographs from hemolytic activity test of the hydrogels. (c) The proliferation of L929 cells for hydrogels. Error bar indicates standard deviation. (d) LIVE/DEAD staining of L929 cells after contact with the hydrogels. Scale bar: 200 μm.

being treated for 3 days. In comparison to the CBM-CBM-CMCS-TA gel and CMCS-TA/FWO2 hydrogel, CBM-CMCS-TA/FWO2 gel + US displayed significant differences (P 0.05). However, no significant difference was found between the CBM-CMCS-TA gel and CMCS-TA/FWO2 hydrogel groups ($P >$ 0.05). After 7 days of treatment, all three hydrogel groups had a significantly higher wound repair rate than the Control and US groups ($P < 0.05$). The wounds in the Control and US groups were largely healed by the 14th day, while the hydrogel group's wounds had entirely healed, and even some of the mice had hair covering them. Additionally, the CBM-CMCS-TA/FWO2 gel + US group's healing rate revealed a significant change from the CBM-CMCS-TA/FWO2 gel group ($P < 0.05$), suggesting that it was inherently advantageous to wound healing. These results were in line with earlier studies showing that CS-based wound dressings combined with US could speed up wound healing. The CBM-CMCS-TA/FWO2 gel + US group displayed the fewest colonies on day 7 following treatment, compared to the other groups (Fig. 5d). This finding suggests that the CBM-CMCS-TA/FWO2 gel + US treatment was effective in killing the bacteria quickly and preventing their growth and further infection of the wound.

3.6 Molecular mechanism of CMCS-TA/FWO2 gel + US promoting wound healing in mice

Inflammation is a normal process of wound healing. Early inflammation is the key to wound healing, but long-term inflammation will prevent the wound from developing into the proliferative stage, resulting in chronic wounds or scars after healing. Hematoxylin and Eosin (H&E) staining was used to observe the skin tissue of the wound on days 7 and 14 after administration, and the morphological changes of the skin layer during the wound healing process were analyzed. On day 3, inflammatory cell infiltration was enhanced in each group. The epidermal growth of the CMCS-TA/FWO2 gel + US group was obvious. On day 7, the wound treated with the CMCS-TA/FWO2 gel + US was covered by epidermal tissue, and the scab began to separate from the epidermis. In contrast, the control and ultrasound groups showed only epidermal tissue (Fig. 6a). It is worth noting that a cuticle appeared in the CMCS-TA/FWO2 gel + US group, indicating that the wound had been completely repaired. For the CMCS-TA gel and CMCS-TA/FWO2 gel, the epidermis almost completely covered the wound and the scab had begun to separate from the epidermis. In contrast, in the control group, the epidermis still extended into the subcutaneous tissue. Finally, on day 14, the stratum corneum continued to form in the CMCS-TA/FWO2 gel + US group, and the stratum corneum in the CMCS-TA and CMCS-TA/FWO2 groups was partially formed but still crusted. In both the control and ultrasound groups, the epidermis had just completely covered the wound area and the vessels were still being repaired (Fig. 6a). These results indicate that CMCS-TA/FWO2 gel + US accelerates the repair of the damaged tissue and promotes epidermalization. The CMCS-TA/FWO2 gel's three-dimensional

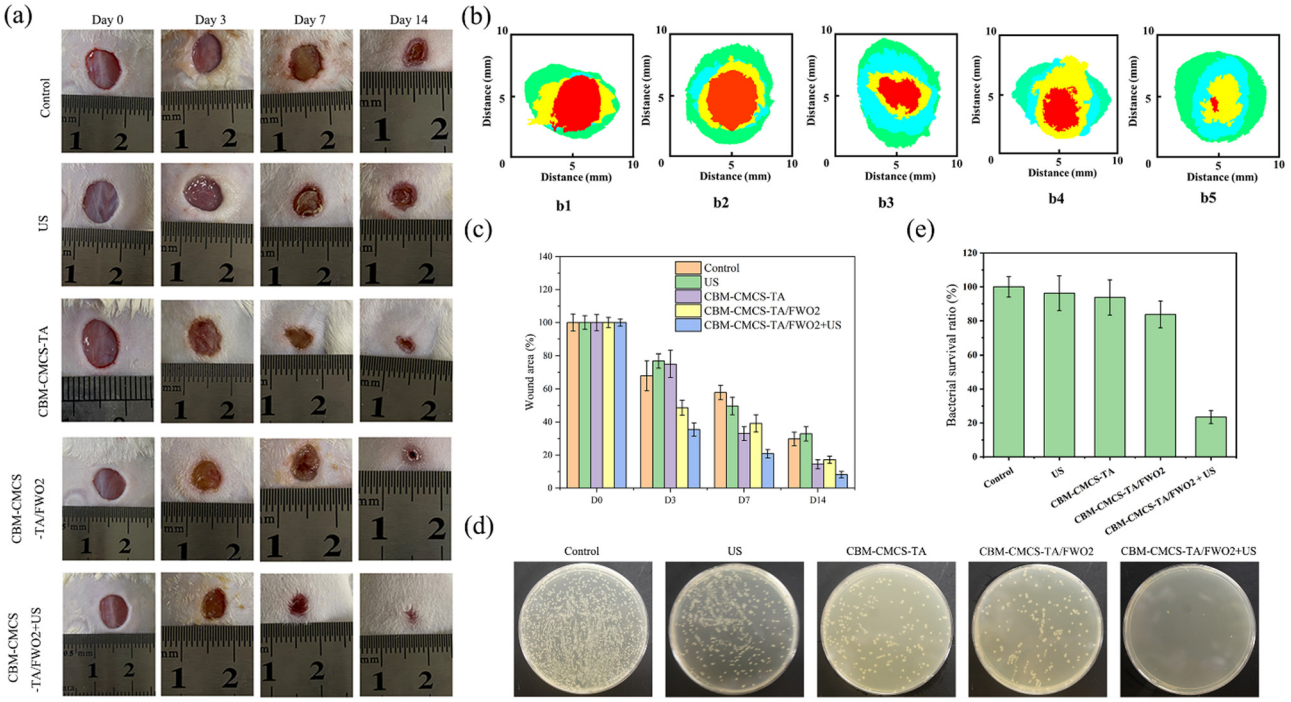

Fig. 5 *In vivo* wound healing efficacy and antibacterial effects of the piezoelectric hydrogels. (a) Photographs of infected wounds of Kunming mice (n = 5/group) at different times after the treatment with PBS, US, CBM-CMCS-TA gel, CBM-CMCS-TA/FWO2 gel, and CBM-CMCS-TA/FWO2 + US. (b) Schematic diagram of wound area during 14 d for (b1) PBS, (b2) US, (b3) CBM-CMCS-TA gel, (b3) CBM-CMCS-TA gel, (b4) CBM-CMCS-TA/FWO2 gel, and (b5) CBM-CMCS-TA/FWO2 + US. (c) Quantitative analysis of the wound area in different groups. (d) Photographs of bacterial colonies formed on LB agar plates on day 7 after different treatments (diluted 10^7 times, n = 3/group). (e) Corresponding bacterial survival rate on day 7. Data are expressed as mean ± S.E.M. ns indicates no significant difference. A significant difference at $^*P < 0.05$, $^{**}P < 0.01$, $^{***}P < 0.001$ level was compared with the control group.

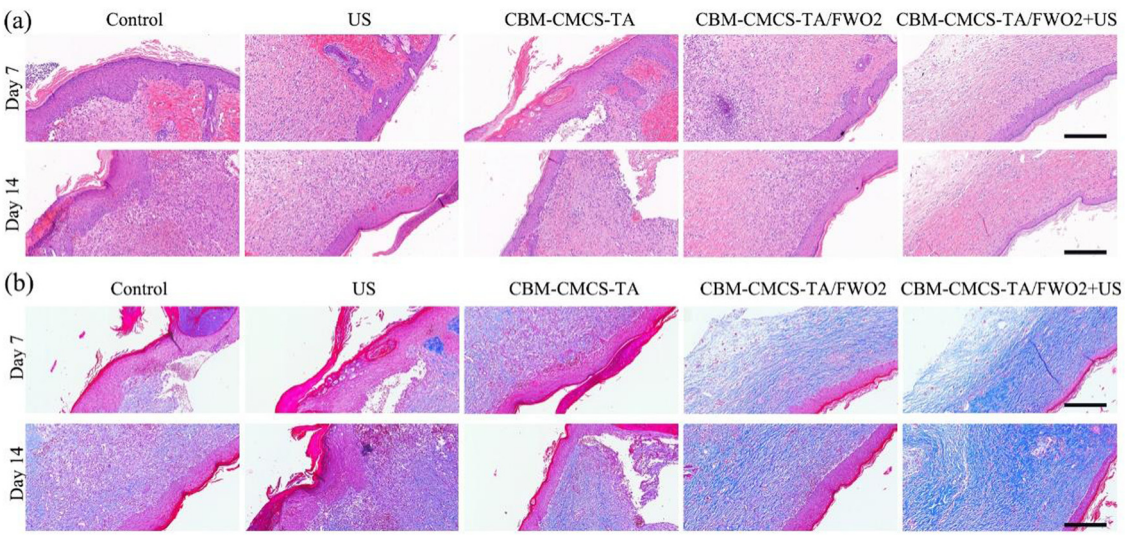

Fig. 6 Wound closure performance and *in vivo* host response evaluation of the piezoelectric hydrogel. (a) Representative images of H&E staining and (b) Masson trichrome staining of harvested healing skins at day 7 and day 14 post-surgery. Scale bar: 100 μm.

network structure facilitates gas exchange while maintaining fluid balance at the wound site. In addition, the porous structure accurately mimics the composition and functionality of the extracellular matrix (ECM), which can aid in cell migration, maturation, and growth. It is clear that the CMCS-TA/FWO2 gel + US group encourages skin epidermalization, and the development of the stratum corneum, and is favorable to scab formation. The CMCS-TA/FWO2 gel + US group can also effectively promote the transformation from the inflammatory phase to the proliferative phase and promote the process of wound healing.

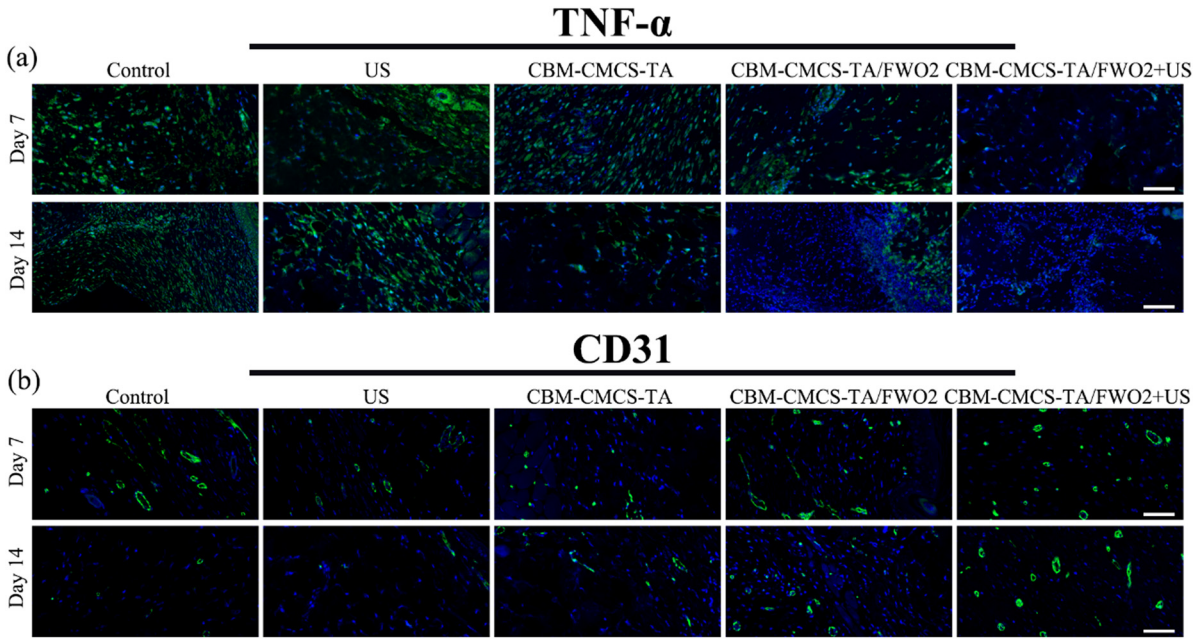

Fig. 7 TNF-α and CD31 expression during the wound healing process. (a) Representative immunofluorescence images of regenerated wound tissues on day 7 and day 14 after labeled with TNF-α (green) and (b) CD31. Scale bar: 50 μm.

The final stage of wound healing determines whether scarring will occur or whether the wound will recur. The remodeling phase involves regression of neovascularization, as well as periodic deposition into the extracellular matrix, followed by the reconstitution of granulation tissue into the collagenous tissue. Granulation tissue first forms Collagen III, which is partially replaced by stronger Collagen I as wound remodeling proceeds. Collagen production can promote re-epithelialization and thus wound healing. The repair of the skin tissue structure at the wound was further explored by Masson staining. The results of Masson staining at the wound on the 7th and 14th days after administration are shown in Fig. 6b. On the 7th day after drug administration, a certain amount of collagen was produced in the wound sites of each group, and there was no significant difference in the amount of collagen. The amount of collagen in the CMCS-TA/FWO2 gel + US group and positive drug (DECB hydrogel) group was slightly higher than that in the control (PBS) group. On day 14, Masson staining exhibited more collagen deposition in the CMCS-TA/FWO2 gel + US group (95.37%), compared with 76.12% in the US group and 76.12% in the control (PBS) group (Fig. 6b). At the same time, the collagen in the CMCS-TA/FWO2 gel + US group was evenly distributed and more complete, indicating that the CMCS-TA/FWO2 gel + US hydrogel could promote wound healing by promoting the production and deposition of collagen.

3.7 *In vivo* anti-inflammatory and antibacterial effects

By utilizing immunofluorescent staining, it is possible to further determine the inflammation, angiogenesis, and re-epithelialization reactions in wound beds. It is believed that persistent inflammation plays a significant role in the slow healing process. TNF-α (tumor necrosis factor) was chosen to assess the effectiveness of these hydrogel dressings in warding off infection. To further reveal the inflammatory response, immunofluorescent staining for TNF-α was carried out. Additionally, the immunofluorescent TNF-α staining sections exhibited that the CBM-CMCS-TA/FWO2 gel + US did not cause as much of an inflammatory reaction. On both the 7th day and the 14th day, the CBM-CMCS-TA/FWO2 gel + US that was loaded with the $FeWO_4$ nanorods demonstrated the decreased expression of TNF-α compared to other groups (Fig. 7a). Both the CBM-CMCS-TA and CBM-CMCS-TA/FWO2 groups significantly differed from the Tegaderm films group, demonstrating that these hydrogels have more beneficial effects than the control group. The development of a vascular network is a crucial sign that a wound is healing. When comparing the CBM-CMCS-TA/FWO2 gel + US group to the PBS-treated group at day 21, immunohistochemical staining of CD31 revealed that there is unmistakably more vasculature produced at the wounds treated with the CMCS-TA/FWO2 gel + US. Furthermore, the CMCS-TA/FWO2 gel + US treated group has larger, more developed microvessels at day 21 (Fig. 7b and c). Therefore, in particular, the CMCS-TA/FWO2 gel + US treated group significantly enhanced wound closure and caused a better healing efficiency than the Tegaderm films by downregulating proinflammatory factor (TNF-α) expression and upregulating production of CD31 concurrently.

4. Conclusion

In summary, the distinct piezoelectric composite hydrogels with high adhesion ability, favorable biocompatibility, and desirable antibacterial function were rationally designed and engineered by cross-linking CMCS with carboxymethyl chitosan, TA, carbomer,

and piezoelectric $FeWO_4$ antibacterial nanoagent. The hydrogels exhibited rheological stability, proper swelling, degradability as well as antibacterial activity induced by US. The synergistic coupling of the US acoustic cavitation effect with the electric field built into the piezoelectric $FeWO_4$ generates an abundance of ROS through increased carrier generation, separation, and transfer. The prepared hydrogels achieved high bactericidal and antitoxic activities due to the produced cytotoxic ROS. In addition, *in vivo* experiments have proved that the piezoelectric hydrogel in collaboration with US can significantly promote the healing of full-thickness skin wounds in mice infected by bacteria regulating inflammation, accelerating collagen deposition, and promoting vascularization. In particular, the histomorphological evaluation and expressions of TNF-α and CD31 revealed that piezoelectric hydrogel induced a better-promoting effect on wound healing. These results indicate that piezoelectric hydrogels with multiple functions are desirable candidates for wound healing dressing.

Author contributions

Min Xu: conceptualization, investigation, data curation, formal analysis, methodology, validation, and writing the original draft. Shaozhen Wu, Li Ding, Caijiao Lu: investigation and validation. Huangjing Qian: supervision, writing the review, and editing. Jinmiao Qu: supervision, writing the review, and editing. Yu Chen: conceptualization, writing review, editing, and funding acquisition.

Conflicts of interest

There are no conflicts to declare.

Acknowledgements

This work was financially supported by the Shanghai Science and Technology Program (Grant No. 21010500100), Wenzhou Science and Technology Planning Project (Grant No. Y20210245), Basic Research Program of Shanghai Municipal Government (Grant No. 21JC1406002) and Exploration Funding of Wenzhou Institute of Shanghai University.

Notes and references

1 A.-G. Niculescu and A. M. Grumezescu, An Up-to-Date Review of Biomaterials Application in Wound Management, *Polymers*, 2022, **14**(3), 421.
2 H. Sorg, D. J. Tilkorn, S. Hager, J. Hauser and U. Mirastschijski, Skin Wound Healing: An Update on the Current Knowledge and Concepts, *Eur. Surg. Res.*, 2017, **58**(1–2), 81–94.
3 P.-H. Wang, B.-S. Huang, H.-C. Horng, C.-C. Yeh and Y.-J. Chen, Wound healing, *J. Chin. Med. Assoc.*, 2018, **81**(2), 94–101.
4 A. Leung, T. M. Crombleholme and S. G. Keswani, Fetal wound healing: implications for minimal scar formation, *Curr. Opin. Pediatr.*, 2012, **24**(3), 371–378.
5 G. Han and R. Ceilley, Chronic Wound Healing: A Review of Current Management and Treatments, *Adv. Ther.*, 2017, **34**(3), 599–610.
6 M. Mirhaj, S. Labbaf, M. Tavakoli and A. Seifalian, An Overview on the Recent Advances in the Treatment of Infected Wounds: Antibacterial Wound Dressings, *Macromol. Biosci.*, 2022, **22**(7), e2200014.
7 X. Ji, G. Liu, Y. Cui, W. Jia, Y. Luo and Z. Cheng, A hybrid system of hydrogel/frog egg-like microspheres accelerates wound healing via sustained delivery ofRCSPs, *J. Appl. Polym. Sci.*, 2020, **137**(46), 49521.
8 L. Qi, C. Zhang, B. Wang, J. Yin and S. Yan, Progress in Hydrogels for Skin Wound Repair, *Macromol. Biosci.*, 2022, **22**(7), e2100475.
9 Z. Xu, S. Han, Z. Gu and J. Wu, Advances and Impact of Antioxidant Hydrogel in Chronic Wound Healing, *Adv. Healthcare Mater.*, 2020, **9**(5), e1901502.
10 V. Patrulea, V. Ostafe, G. Borchard and O. Jordan, Chitosan as a starting material for wound healing applications, *Eur. J. Pharm. Biopharm.*, 2015, **97**, 417–426.
11 Y. Zhang, M. Jiang, Y. Zhang, Q. Cao, X. Wang, Y. Han, G. Sun, Y. Li and J. Zhou, Novel lignin–chitosan-PVA composite hydrogel for wound dressing, *Mater. Sci. Eng., C*, 2019, 104.
12 Q. Hui, L. Zhang, X. Yang, B. Yu, Z. Huang, S. Pang, Q. Zhou, R. Yang, W. Li, L. Hu, X. Li, G. Cao and X. Wang, Higher Biostability of rh-aFGF-Carbomer 940 Hydrogel and Its Effect on Wound Healing in a Diabetic Rat Model, *ACS Biomater. Sci. Eng.*, 2018, **4**(5), 1661–1668.
13 M. Xu, M. Sun, H. Qiao, Q. Ping and E. S. Elamin, Preparation and evaluation of colon adhesive pellets of 5-aminosalicylic acid, *Int. J. Pharm.*, 2014, **468**(1–2), 165–171.
14 F. Hayati, S. M. Ghamsari, M. M. Dehghan and A. Oryan, Effects of carbomer 940 hydrogel on burn wounds: an in vitro and in vivo study, *J. Dermatol. Treat.*, 2018, **29**(6), 593–599.
15 X. Huang, J. Yang, R. Zhang, L. Ye, M. Li and W. Chen, Phloroglucinol Derivative Carbomer Hydrogel Accelerates MRSA-Infected Wounds' Healing, *Int. J. Mol. Sci.*, 2022, **23**(15), 8682.
16 Y. Huang, F. Shi, L. Wang, Y. Yang, B. M. Khan, K. L. Cheong and Y. Liu, Preparation and evaluation of Bletilla striata polysaccharide/carboxymethyl chitosan/Carbomer 940 hydrogel for wound healing, *Int. J. Biol. Macromol.*, 2019, **132**, 729–737.
17 Y. Zhang, F. He and X. Li, Three-dimensional composite hydrogel based on polyamine zirconium oxide, alginate and tannic acid with high performance for Pb(II), Hg(II) and Cr(VI) trapping, *J. Taiwan Inst. Chem. Eng.*, 2016, **65**, 304–311.
18 S. Ge, N. Ji, S. Cui, W. Xie, M. Li, Y. Li, L. Xiong and Q. Sun, Coordination of Covalent Cross-Linked Gelatin Hydrogels via Oxidized Tannic Acid and Ferric Ions with Strong Mechanical Properties, *J. Agric. Food Chem.*, 2019, **67**(41), 11489–11497.

19 D. E. Payne, N. R. Martin, K. R. Parzych, A. H. Rickard, A. Underwood and B. R. Boles, Tannic Acid Inhibits Staphylococcus aureus Surface Colonization in an IsaA-Dependent Manner, *Infect. Immun.*, 2013, **81**(2), 496–504.

20 N. Li, X. Yang, W. Liu, G. Xi, M. Wang, B. Liang, Z. Ma, Y. Feng, H. Chen and C. Shi, Tannic Acid Cross-linked Polysaccharide-Based Multifunctional Hemostatic Microparticles for the Regulation of Rapid Wound Healing, *Macromol. Biosci.*, 2018, **18**(11), e1800209.

21 X. Zhou, Q. Zhou, Q. Chen, Y. Ma, Z. Wang, L. Luo, Q. Ding, H. Li and S. Tang, Carboxymethyl Chitosan/Tannic Acid Hydrogel with Antibacterial, Hemostasis, and Antioxidant Properties Promoting Skin Wound Repair, *ACS Biomater. Sci. Eng.*, 2023, **9**(1), 437–448.

22 S. Shakya, Y. He, X. Ren, T. Guo, A. Maharjan, T. Luo, T. Wang, R. Dhakhwa, B. Regmi, H. Li, R. Gref and J. Zhang, Ultrafine Silver Nanoparticles Embedded in Cyclodextrin Metal-Organic Frameworks with GRGDS Functionalization to Promote Antibacterial and Wound Healing Application, *Small*, 2019, **15**(27), e1901065.

23 Y. Liang, X. Zhao, T. Hu, B. Chen, Z. Yin, P. X. Ma and B. Guo, Adhesive Hemostatic Conducting Injectable Composite Hydrogels with Sustained Drug Release and Photothermal Antibacterial Activity to Promote Full-Thickness Skin Regeneration During Wound Healing, *Small*, 2019, **15**(12), e1900046.

24 S. Panda, T. K. Rout, A. D. Prusty, P. M. Ajayan and S. Nayak, Electron Transfer Directed Antibacterial Properties of Graphene Oxide on Metals, *Adv. Mater.*, 2018, **30**(7), 1702149.

25 Q. Xin, H. Shah, A. Nawaz, W. Xie, M. Z. Akram, A. Batool, L. Tian, S. U. Jan, R. Boddula, B. Guo, Q. Liu and J. R. Gong, Antibacterial Carbon-Based Nanomaterials, *Adv. Mater.*, 2019, **31**(45), e1804838.

26 Y. M. You, W. Q. Liao, D. Zhao, H. Y. Ye, Y. Zhang, Q. Zhou, X. Niu, J. Wang, P. F. Li, D. W. Fu, Z. Wang, S. Gao, K. Yang, J. M. Liu, J. Li, Y. Yan and R. G. Xiong, An organic-inorganic perovskite ferroelectric with large piezoelectric response, *Science*, 2017, **357**(6348), 306–309.

27 J. Wu, N. Qin and D. Bao, Effective enhancement of piezocatalytic activity of $BaTiO_3$ nanowires under ultrasonic vibration, *Nano Energy*, 2018, **45**, 44–51.

28 Y. Zhang, W. Ng, J. Hu, S. S. Mussa, Y. Ge and H. Xu, Formulation and in vitro stability evaluation of ethosomal carbomer hydrogel for transdermal vaccine delivery, *Colloids Surf., B*, 2018, **163**, 184–191.

29 I. A. Duceac, L. Verestiuc, C. D. Dimitriu, V. Maier and S. Coseri, Design and Preparation of New Multifunctional Hydrogels Based on Chitosan/Acrylic Polymers for Drug Delivery and Wound Dressing Applications, *Polymers*, 2020, **12**(7), 1473.

30 X. Feng, X. Hou, C. Cui, S. Sun, S. Sadik, S. Wu and F. Zhou, Mechanical and antibacterial properties of tannic acid-encapsulated carboxymethyl chitosan/polyvinyl alcohol hydrogels, *Eng. Regener.*, 2021, **2**(0), 57–62.

31 C. Ghobril and M. W. Grinstaff, The chemistry and engineering of polymeric hydrogel adhesives for wound closure: a tutorial, *Chem. Soc. Rev.*, 2015, **44**(7), 1820–1835.

32 M. Wu, Z. Zhang, Z. Liu, J. Zhang, Y. Zhang, Y. Ding, T. Huang, D. Xiang, Z. Wang, Y. Dai, X. Wan, S. Wang, H. Qian, Q. Sun and L. Li, Piezoelectric nanocomposites for sonodynamic bacterial elimination and wound healing, *Nano Today*, 2021, **37**, 101104.

33 Y. Liang, B. Chen, M. Li, J. He, Z. Yin and B. Guo, Injectable Antimicrobial Conductive Hydrogels for Wound Disinfection and Infectious Wound Healing, *Biomacromolecules*, 2020, **21**(5), 1841–1852.